Electronic Supplementary Material (ESI) for Journal of Materials Chemistry A.

Electronic Supplementary Information

Chemical interactions between red P and functional groups in NiP_3/CNT composite anodes for enhanced sodium storage

Muhammad Ihsan Ul Haq,[a] He Huang,[a] Jiang Cui,[a] Shanshan Yao,[a] Junxiong Wu,[a] Woon Gie Chong,[a] Baoling Huang*[a] and Jang-Kyo Kim *[a]

[a] Department of Mechanical and Aerospace Engineering, The Hong Kong University of Science and Technology, Clear Water Bay, Hong Kong, China.

* Corresponding author information:
E-mail: mebhuang@ust.hk (Baoling Huang)
E-mail: mejkkim@ust.hk (Jang-Kyo Kim)

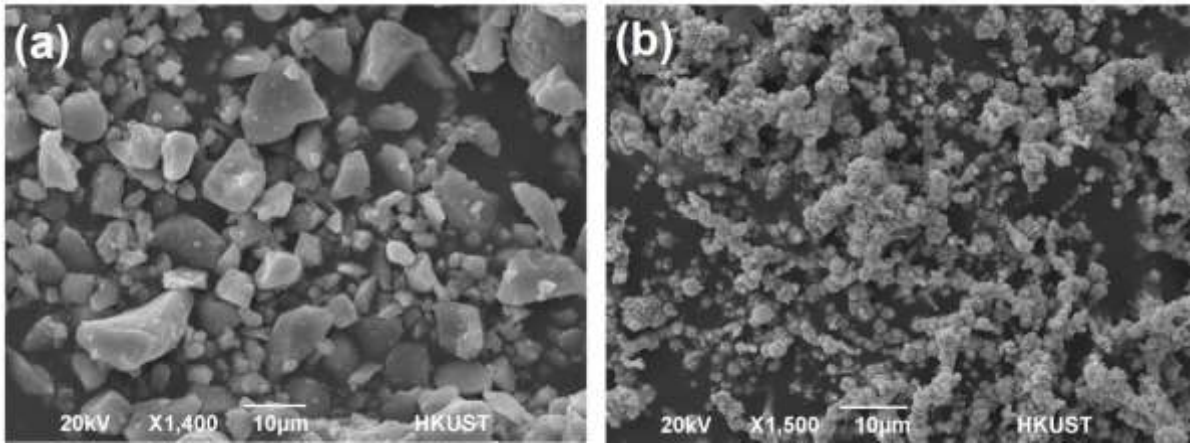

Fig. S1. SEM images of (a) phosphorous powder and (b) nickel powder.

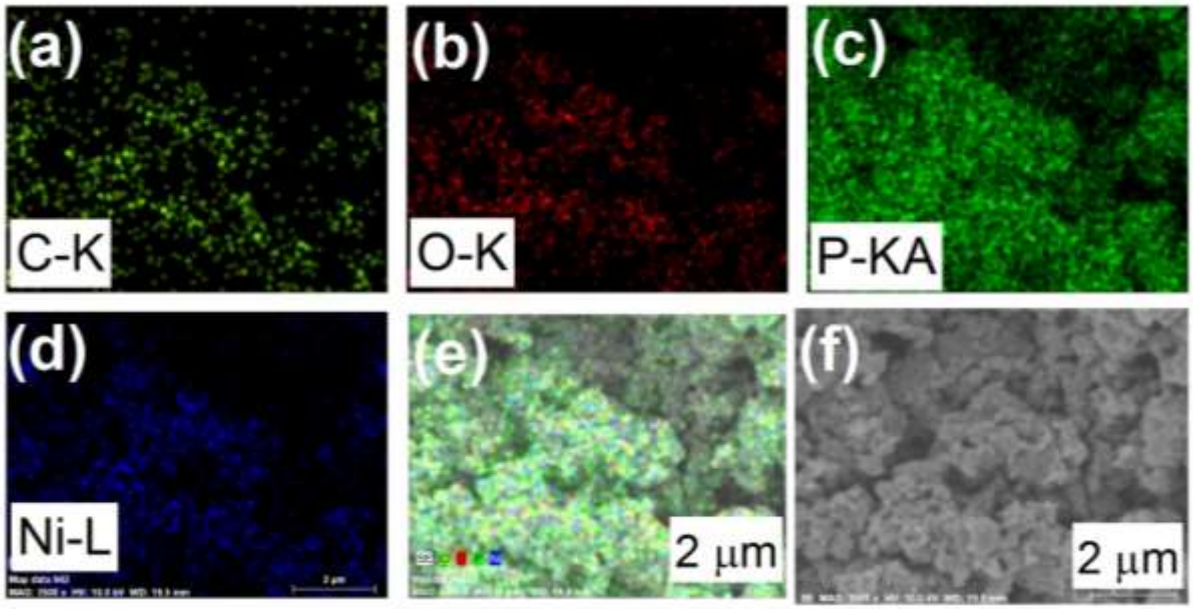

Fig. S2. SEM-EDS elemental maps of NiP_3/CNT composite: (a) C, (b) O, (c) P, (d) Ni, (e) combination of C, O, P and Ni; and (e) the corresponding SEM image.

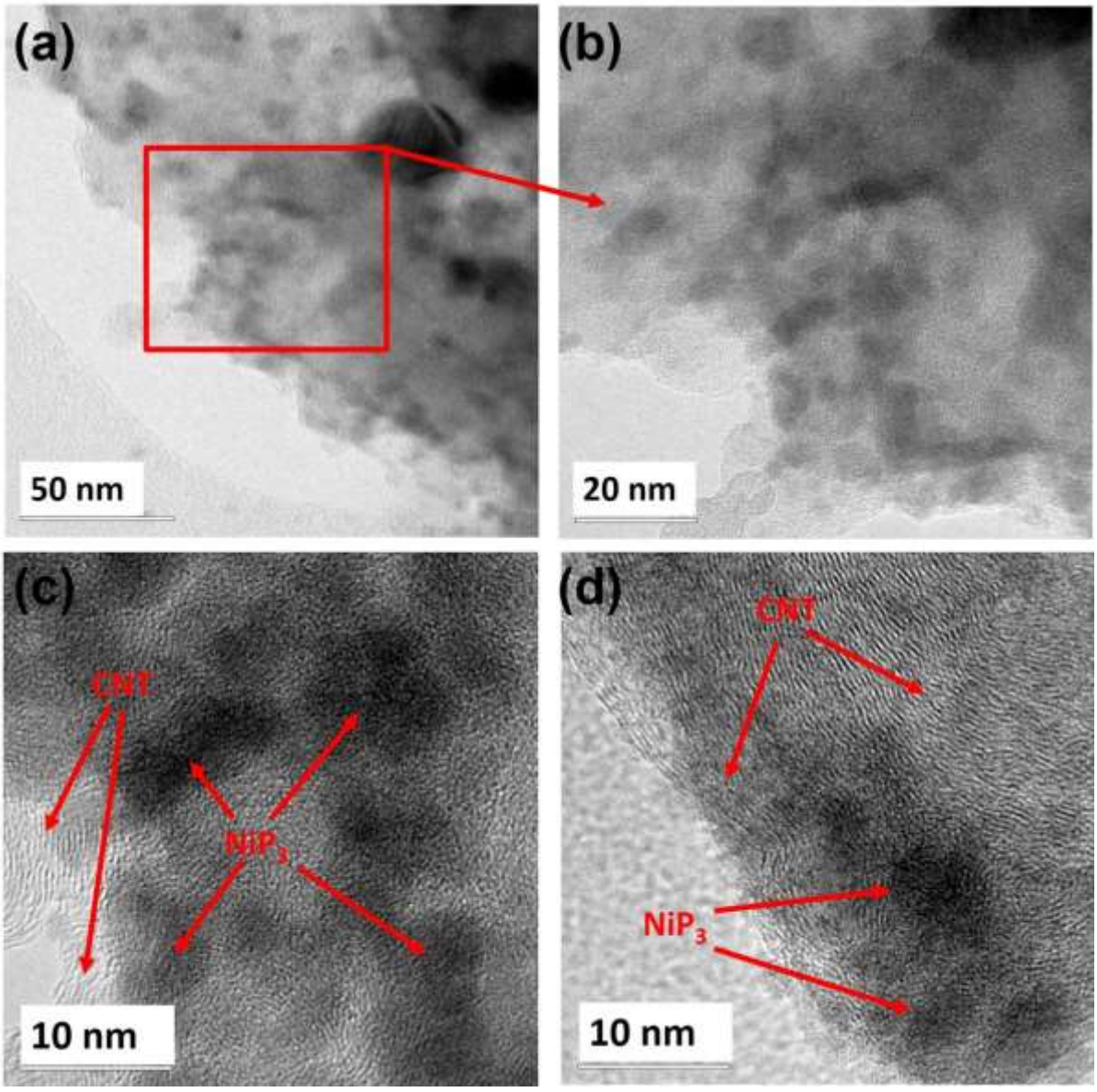

Fig. S3. (a) TEM micrograph and (b-d) magnified views of TEM micrograph of NiP_3/CNT composites.

Table S1. Details of constituent elements obtained from the XRF analysis.

Element	Mol %	Error %
P	70.82	0.9967
Ni	24.42	0.1152
Fe	3.82	0.0896
Cr	0.94	0.1118

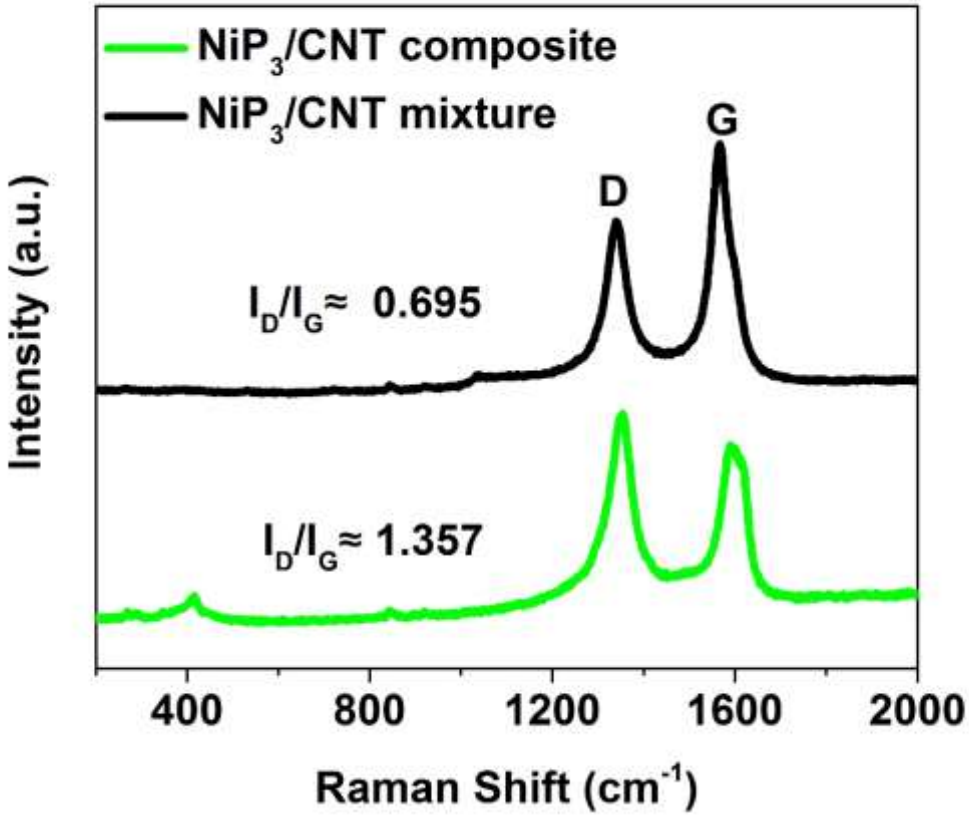

Fig. S4. Raman spectra of NiP_3/CNT composite and NiP_3/CNT mixture.

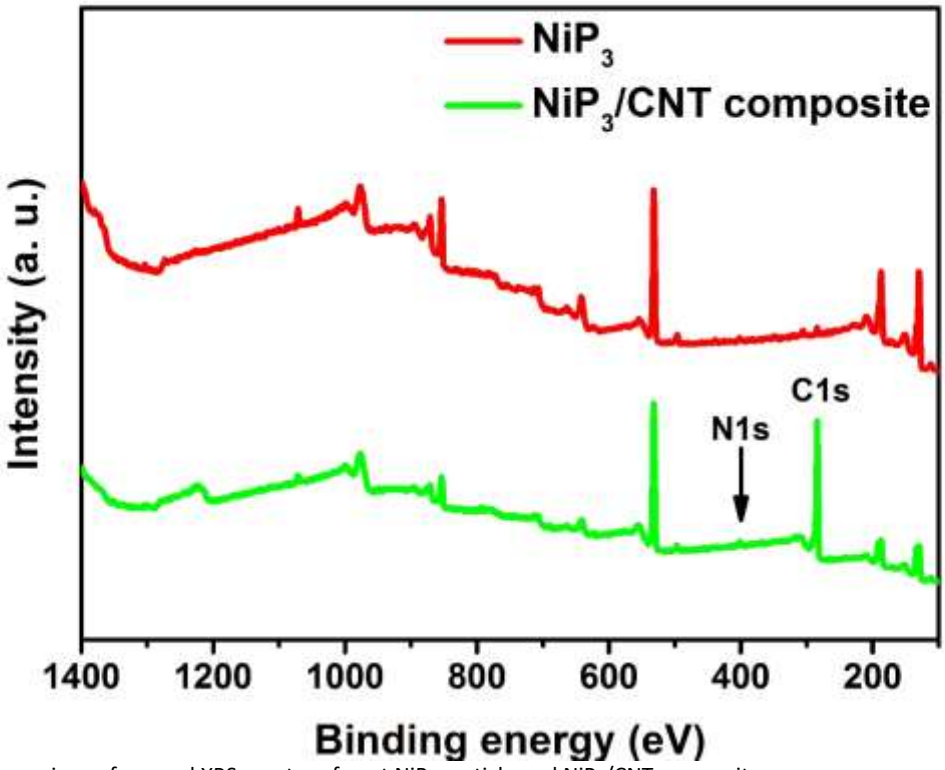

Fig. S5. Comparison of general XPS spectra of neat NiP_3 particle and NiP_3/CNT composite.

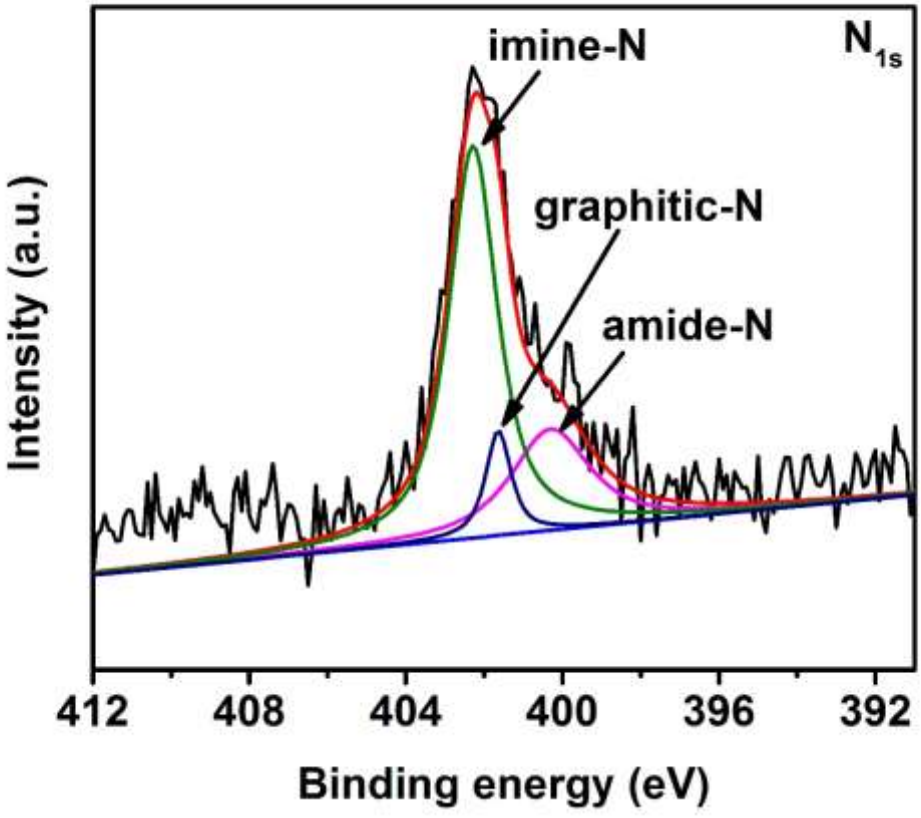

Fig. S6. Deconvolution of high resolution N_{1s} XPS spectrum of NiP_3/CNT composite.

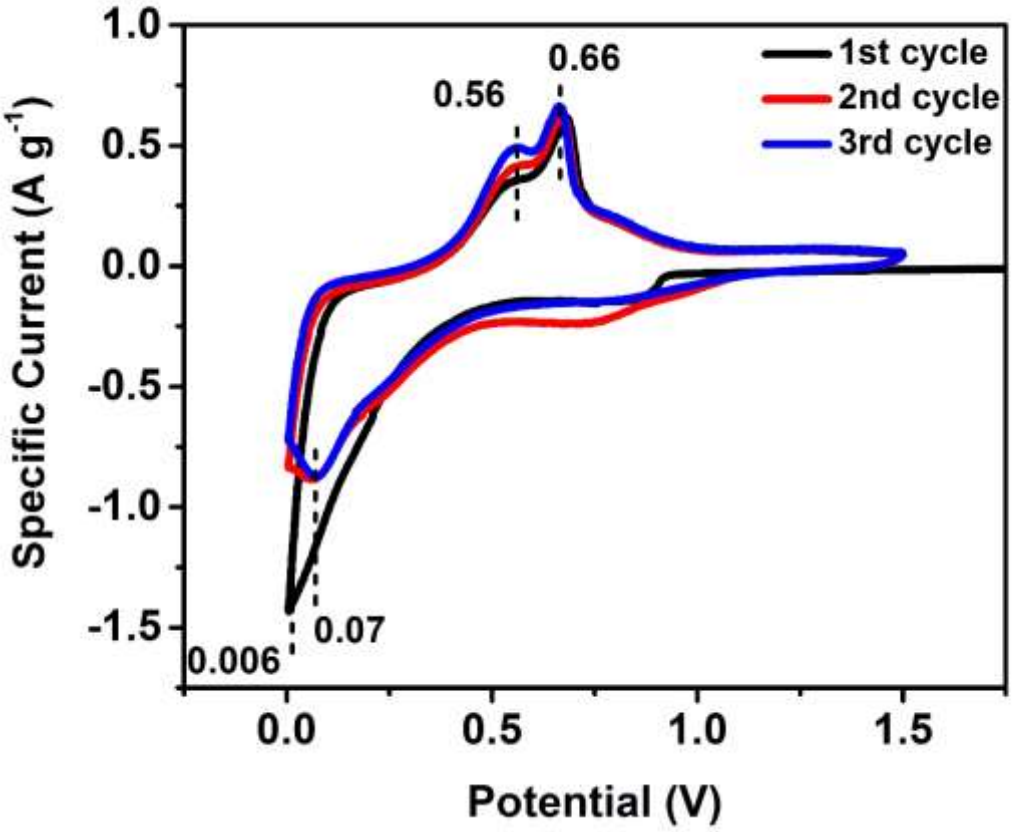

Fig. S7. CV curves of NiP_3 electrode.

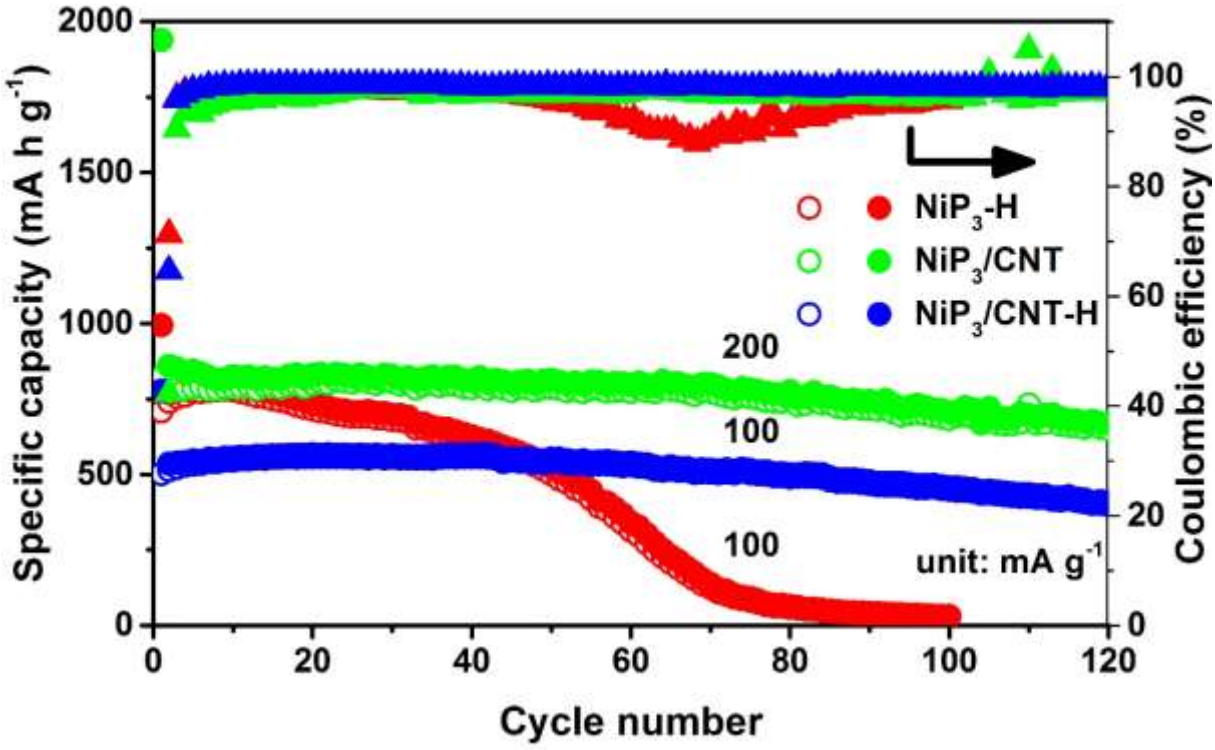

Fig. S8. Comparison of cyclic performance of NiP_3-H, NiP_3/CNT-H at 100 mA g^{-1} and NiP_3/CNT composite electrodes at 200 mA g^{-1}.

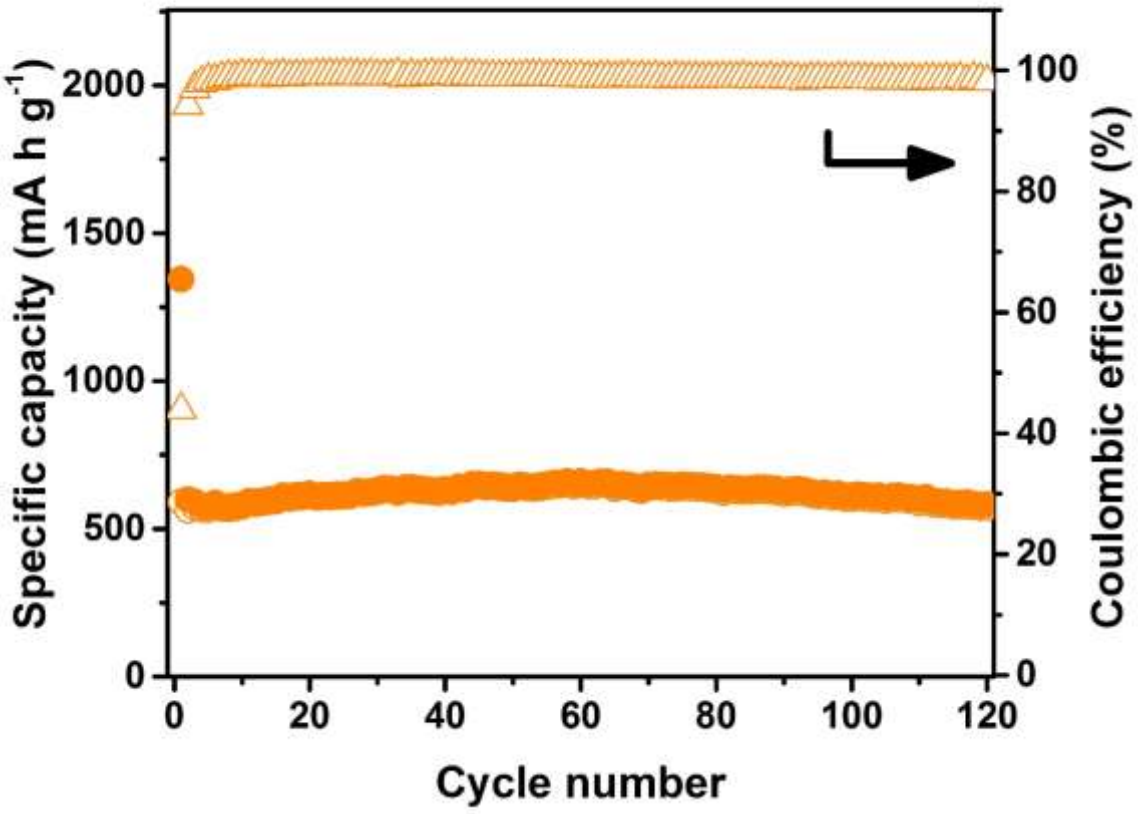

Fig. S9. Cyclic performance of NiP_3/CNT composite electrodes with 30 wt. % of CNTS at 100 mA g^{-1}.

Table S2. Electrochemical performance of transition metal phosphides and their composites prepared by ball milling as anodes for SIBs.

Materials	Cyclic performance			Rate performance		References
	Capacity (mAh g^{-1})	Current density (mA g^{-1})	Cycle number	Capacity (mAh g^{-1})	Current density (mA g^{-1})	
NiP_3	996	100	15	720	1000	S1
CoP	315	100	25	80	2000	S2
FeP	321	50	60	60	500	S3
CuP_2/C	430	150	30	178	2000	S4
CuP_2/C	430	200	100	308	800	S5
FeP/graphite	175	50	70	134	500	S6
P-TiP_2-C	607	200	100	526	800	S7
NiP_3/CNT-H	399	100	120	-	-	
NiP_3/CNT	668	200	120	494	3200	This work
	364	1600	200			

Table S3. Impedance parameters obtained from EIS using the fitting model

Sample	R_e (Ω)	R_{sf+ct} (Ω)	CPE_{sf+dl}	Z_w	C_{int}
NiP_3	5.2	240.2	0.000388	0.003599	0.02335
NiP_3/CNT	6.0	39.9	0.001145	0.01985	0.1174

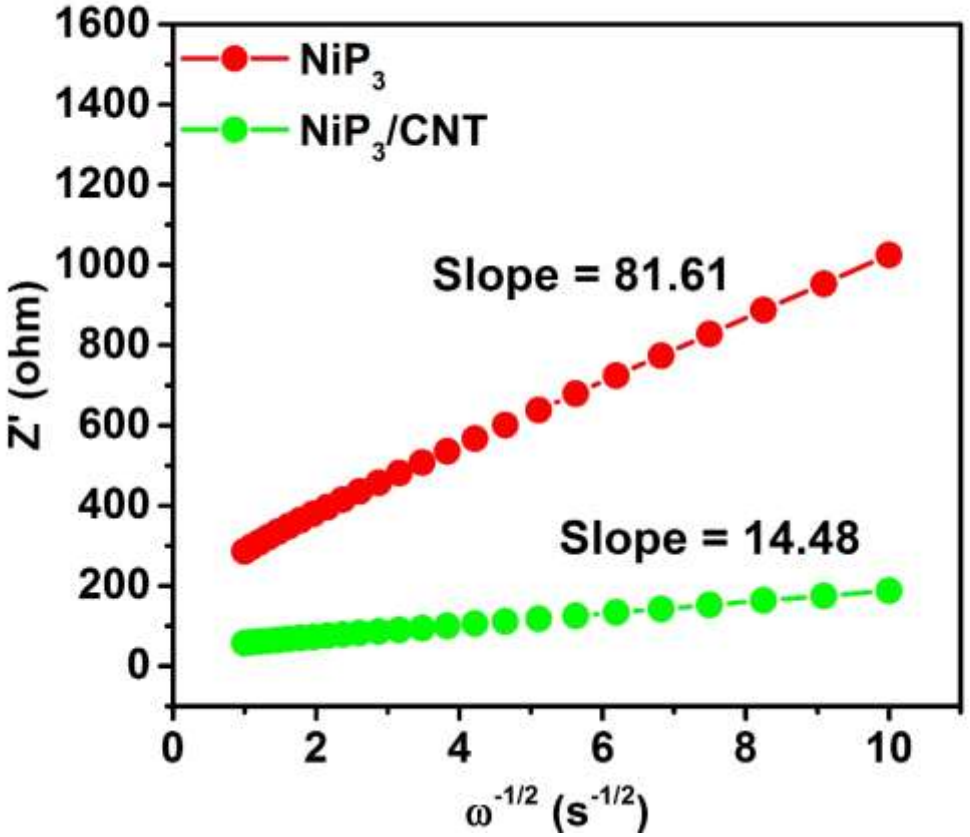

Fig. S10. Z' vs square root of the inverse of frequency used for calculation of Warburg coefficient.

Ex-situ XPS analysis

The *ex-situ* XPS analysis was carried out after the first sodiation and desodiation steps. The P_{2p} peak at ~130 eV related to the Ni–P bond diminished upon the first discharge, indicating the breakage of Ni–P bonds in NiP_3, as shown in Fig. S11. It disappeared upon the first charge due to amorphization of phosphorous which was fully covered by the carbon matrix,[S8] as indicated by the SAED pattern and the *ex-situ* TEM micrographs (Fig. 4 a-d). The peak at ~134.1 eV in the pristine electrode associated with the P–O–C bond upshifted to 134.5 eV upon the first discharge as a result of the formation of Na_3PO_4 phosphate group (Fig. S11). The peak at 134.8 eV also upshifted to 135.3 eV after the first discharge due to formation of $Na_4P_2O_7$ pyrophosphates. The formation of phosphates and pyrophosphates on the electrode surface is considered to be beneficial for improving the rate performance of the composite electrode due to their conductive nature.[S9] The C_{1s} deconvoluted spectrum presents two new peaks emerged at high binding energies of 288.1 and 290.3 eV upon the first discharge and charge processes (Fig. S12). This observation signifies the formation of stable semi-carbonates ($NaCO_3R$) and carbonates of sodium (Na_2CO_3), during which the Na ions were consumed to form an irreversible SEI layer at an initially low Coulombic efficiency. However, these carbonates became stable leading to enhanced Coulombic efficiency in the subsequent cycles.[S8] The deconvolution of Ni_{2p} peaks at 853.5, 861.4, 870.7and 880.8 eV showed an increase in binding energy after the first discharge cycle (Fig. S13). This finding is attributed to the breakage of Ni–P bonds, as evidenced by the vanished P_{2p} peaks at 129.6 and 130.5 eV (Fig. S11). However, the peaks at 856.9 and 874.7 eV showed enhanced oxidation of Ni by forming Ni–O bonds on the electrode surface during the first cycle.

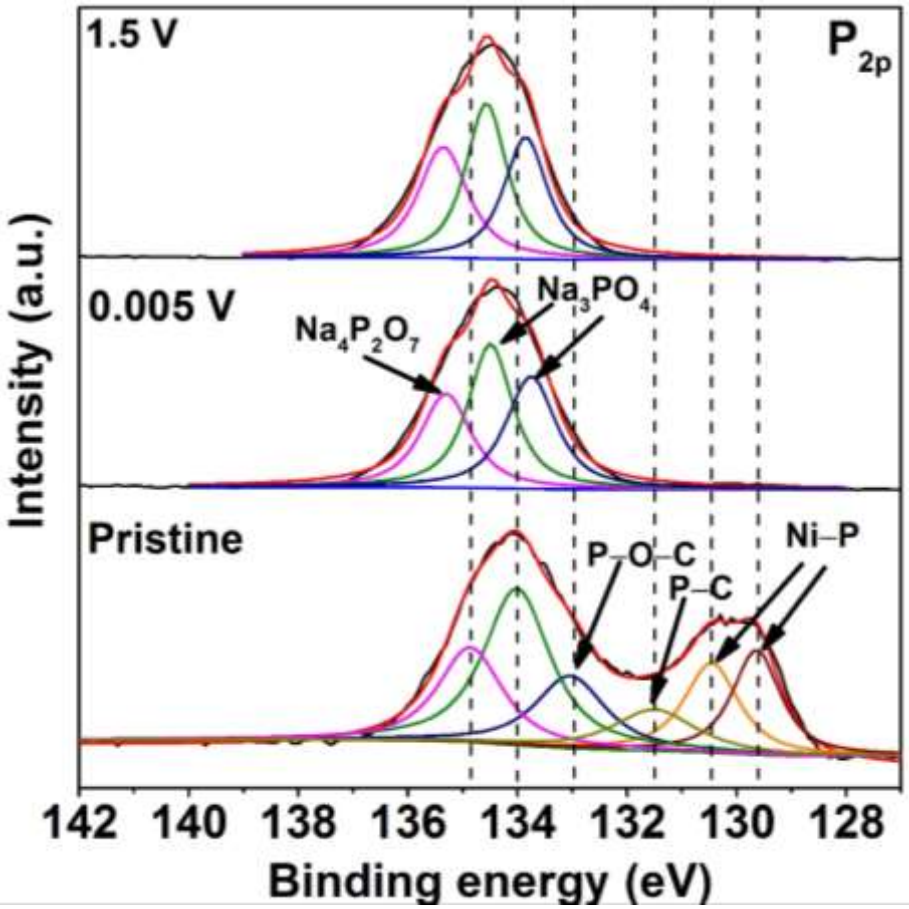

Fig. S11. Comparison of deconvoluted high resolution *ex-situ* XPS spectra of P_{2p} of pristine, sodiated (at 0.005 V) and desodiated (at 1.5 V) NiP_3/CNT composite electrodes.

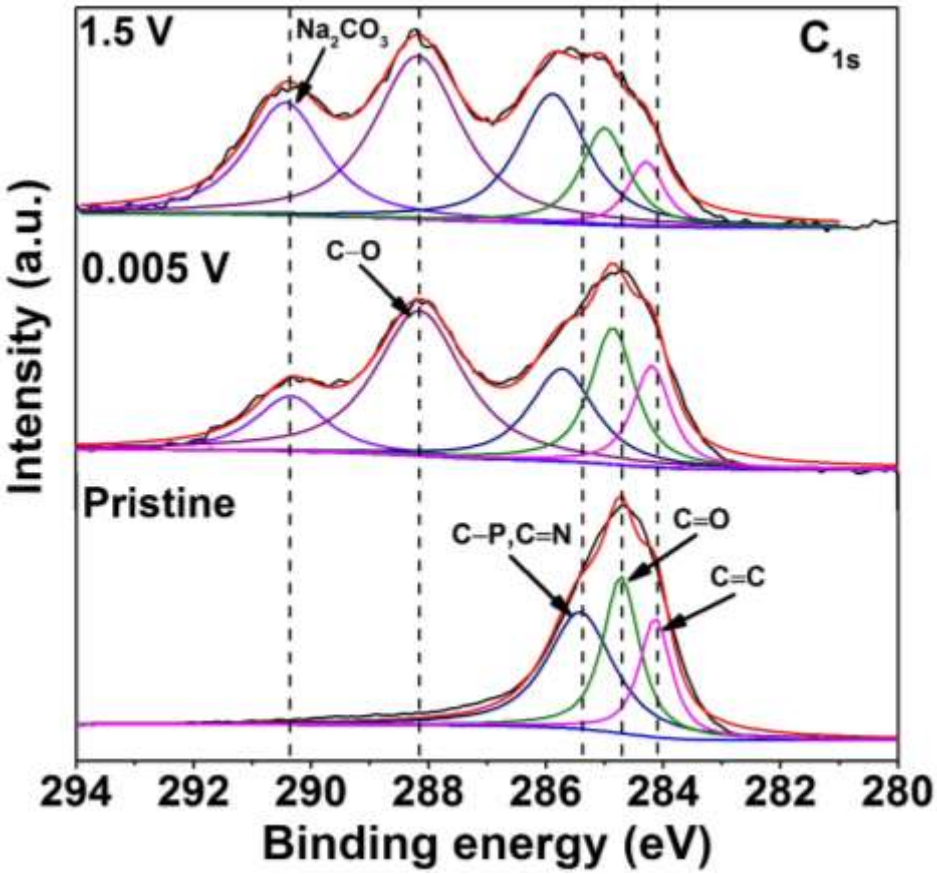

Fig. S12. Comparison of deconvoluted high resolution *ex-situ* XPS spectra of C_{1s} of pristine, sodiated (at 0.005 V) and desodiated (at 1.5 V) NiP_3/CNT composite electrodes.

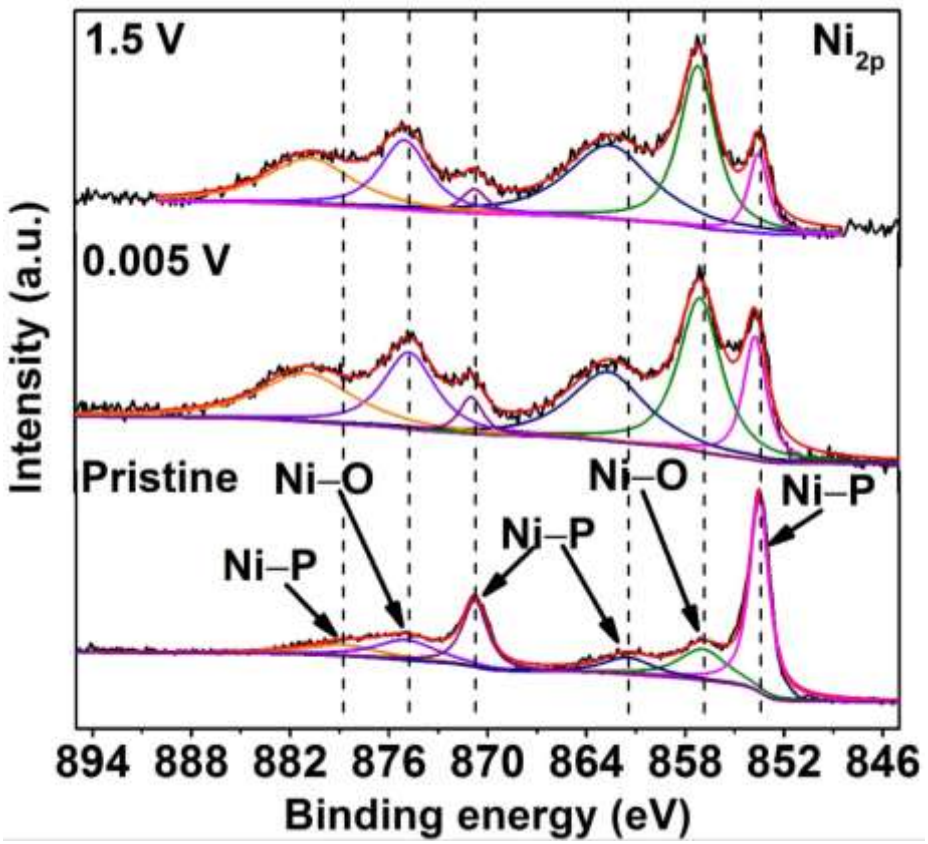

Fig. S13. Comparison of deconvoluted high resolution *ex-situ* XPS spectra of Ni_{2p} of pristine, sodiated (at 0.005 V) and desodiated (at 1.5 V) NiP_3/CNT composite electrodes.

Density Functional Theory (DFT) Calculations

The density functional theory (DFT) calculations were performed based on the first principles using Vienna Ab Simulation Package (VASP)[S10] with a projected augmented wave approach.[S11] The exchange-correlation functional energy was processed by the Perdew-Burke-Ernzerhof (PBE) function within the generalized gradient approximation (GGA).[S10] The thermodynamics of Ni-P stable phases was first considered by constructing an equilibrium Ni–P binary phase diagram based on 0 K DFT calculations, as shown in Fig. S14. The c-Ni_3P, c-$Ni_{12}P_5$, c-Ni_5P_4, c-NiP_2, and c-NiP_3 species (indicated by black dots) were found stable at 0 K with low formation energies. The c-NiP_4 phase (indicated by a red square) was calculated 76 meV/atom above the energy hull, which was decomposed to c-NiP_3 and pure P, showing instability of the c-NiP_4 phase. The P content in the Ni-P binary compounds was worthy of further investigation due to its high theoretical capacity for Na storage. Among the stable Ni–P binary phases, therefore, the c-NiP_3 phase with the highest mole fraction of P was selected in the following discussion. The cut-off energy used for the plane wave expansion of wave function was 520 eV. The 1×1×2 NiP_3 and 3×2×2 graphite supercells were used to form the relevant composite structures. The Brillouin zone was sampled using 5×5×3 meshes for structural optimization to calculate the electronic density of states (DOS). The convergence accuracies for the total energy and force were set at 10^{-5} eV and 0.02 eV/ Å, respectively. Due to the high cost of *ab-initio* molecular dynamics (AIMD) methods, [S12] gamma-point-only sampling of k-space was used in the AIMD simulations for all cases. The AIMD simulations were performed in NVT ensembles with Nosé-Hoover thermostats at 800 K. In each case, a time interval of 2 ps was applied and the total simulation time was set at 8 ps. Charge density differences were calculated using Equation (S1), where, x was either the pristine, –O, –OH, $–NH_2$ or –COOH functional group. The light blue and yellow isosurfaces in charge density difference plots represent depletion and accumulation of charge, respectively, with iso value of 0.01 electron $Bohr^{-3}$.

$$\Delta\rho = \rho_{NiP3/x-graphite} - \rho_{NiP3} - \rho_{NiP3} \quad \text{(S1)}$$

c-NiP_3 crystallized in a cubic structure with a lattice parameter of 7.8 Å, in which each Ni atom was linked to 6 nearest P atoms, forming 8 octahedrons linking with each other in the unit cell, as shown in Fig. S15 (a). For the 3×2×1 pristine graphite layered supercell with AB stacking, the lattice parameters were optimized to show 7.4, 8.4 and 6.9 Å along the *a*-axis, *b*-axis and *c*-axis, respectively.

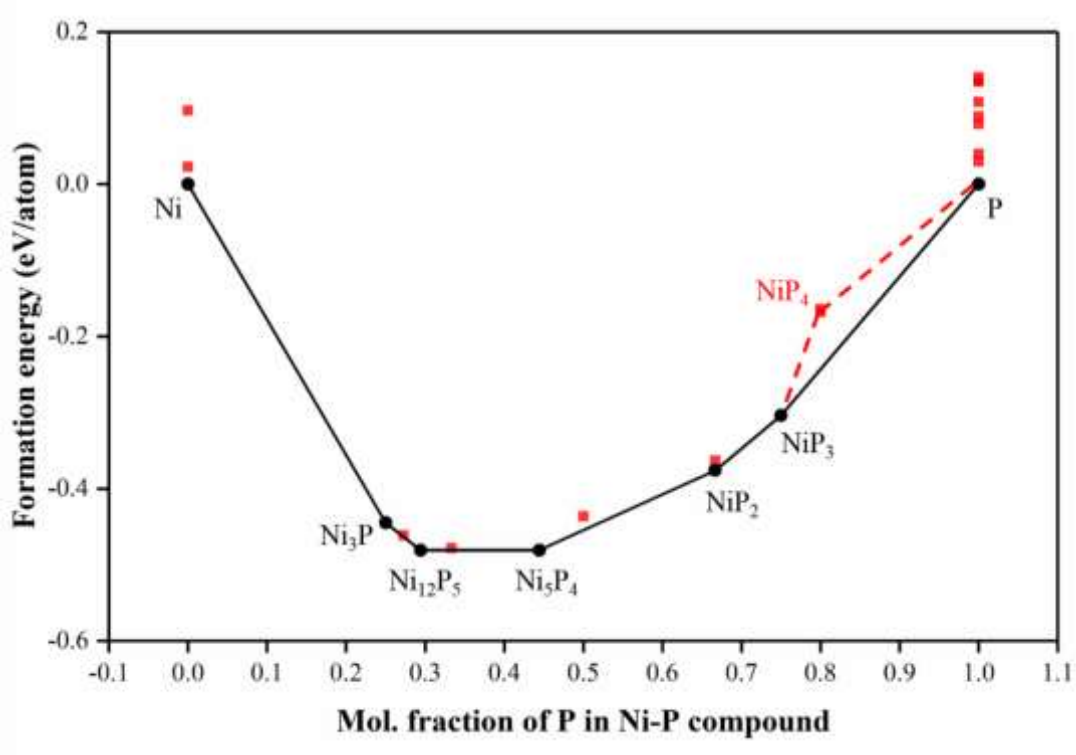

Fig. S14. Equilibrium Ni-P binary phase diagram based on DFT calculations. The black dots indicate stable existence of species at 0 K, while the red squares indicate unstable state above the energy hull. The red dash line refers to the path generation of c-NiP_4.

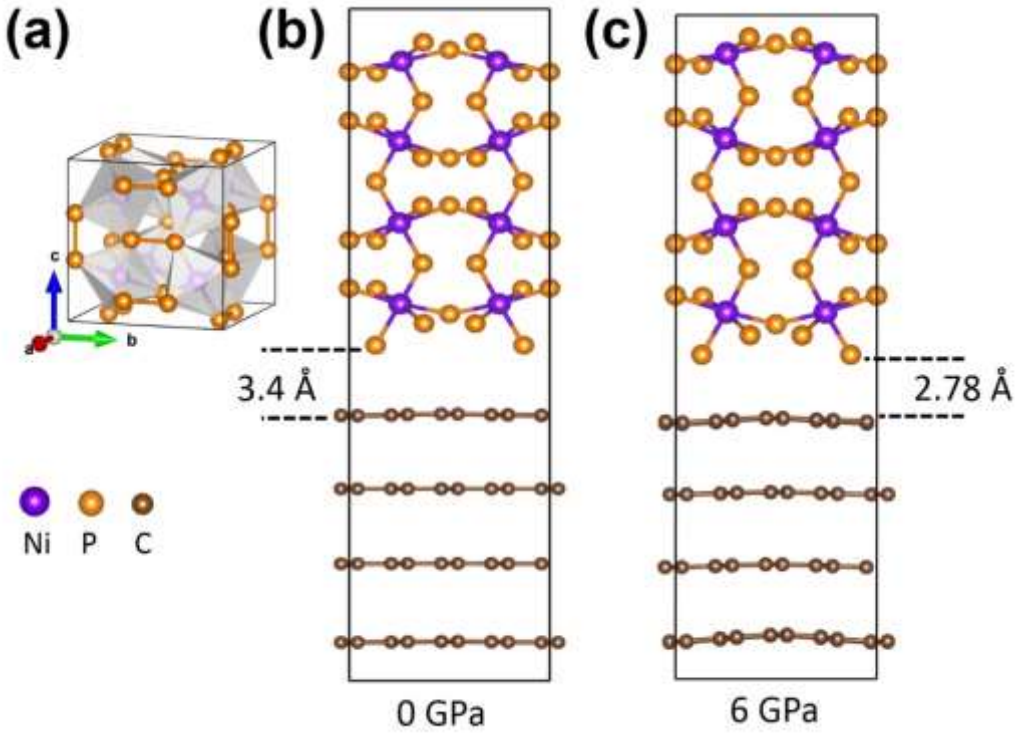

Fig. S15. (a) The unit cell structure of NiP_3; and (b) the lattice configurations of NiP_3/pristine graphite under no pressure and an isostatic pressure of 6 GPa. The atomic distances of P and the nearest C are shown.

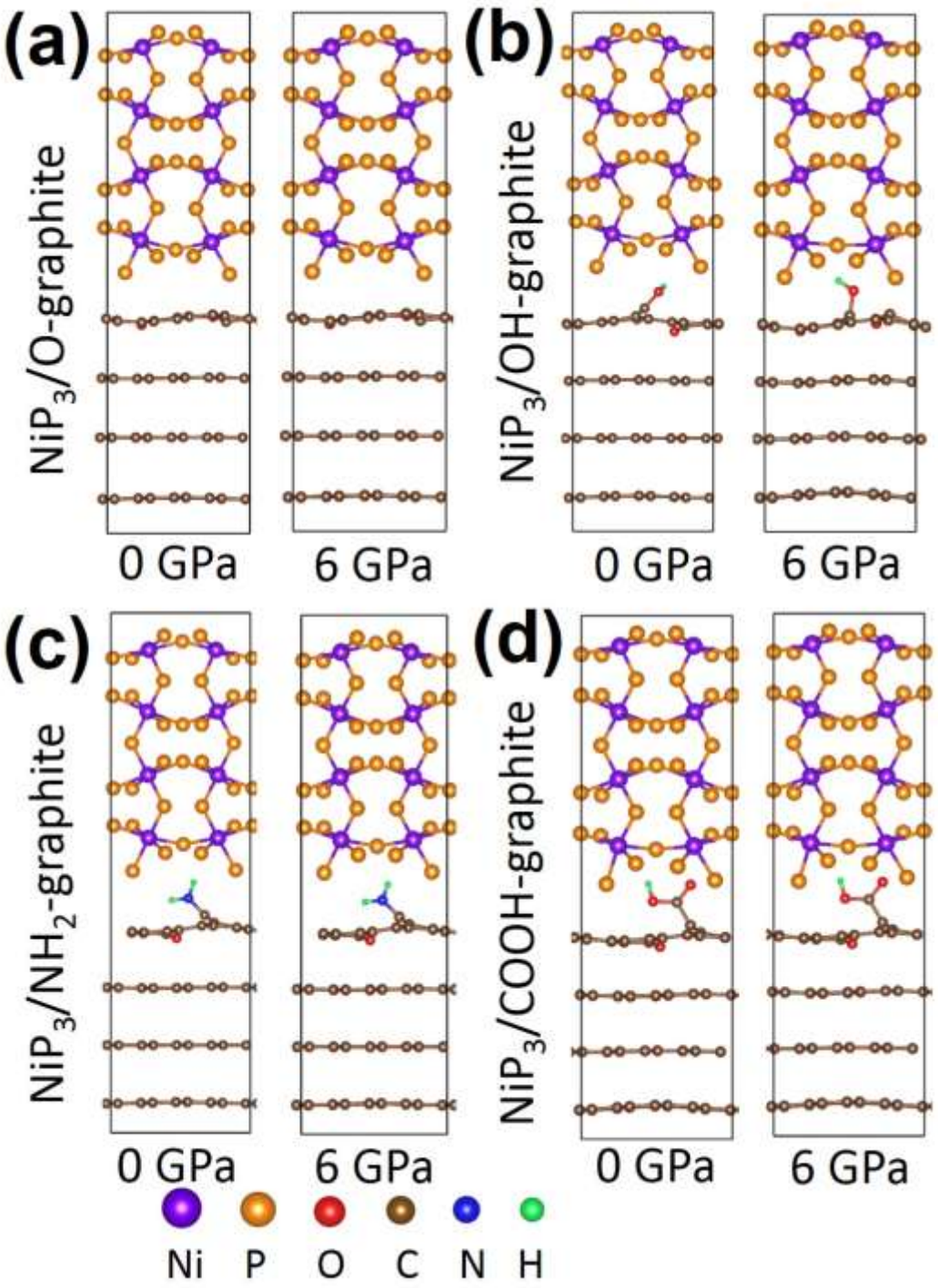

Fig. S16. The initial optimized structural configurations of (a) NiP_3/O-graphite, (b) NiP_3/OH-graphite, (c) NiP_3/NH_2-graphite, and (d) NiP_3/COOH-graphite under no pressure and an isostatic pressure of 6 GPa.

Table S4. Lattice parameters of NiP_3/pristine graphite, NiP_3/O-graphite, NiP_3/OH-graphite, NiP_3/NH_2-graphite, and NiP_3/COOH-graphite with and without an isostatic pressure of 6 GPa.

Condition	No pressure			Isostatic pressure of 6 GPa		
Lattice information	a (Å)	b (Å)	c (Å)	a (Å)	b (Å)	c (Å)
NiP_3/G	7.46	8.42	31.43	7.41	8.36	28.57
NiP_3/O-G	7.47	8.40	30.69	7.43	8.33	28.26
NiP_3/OH-G	7.45	8.42	31.14	7.42	8.33	28.50
NiP_3/NH_2-G	7.46	8.41	31.44	7.42	8.35	28.67
NiP_3/COOH-G	7.40	8.37	29.11	7.39	8.31	28.11

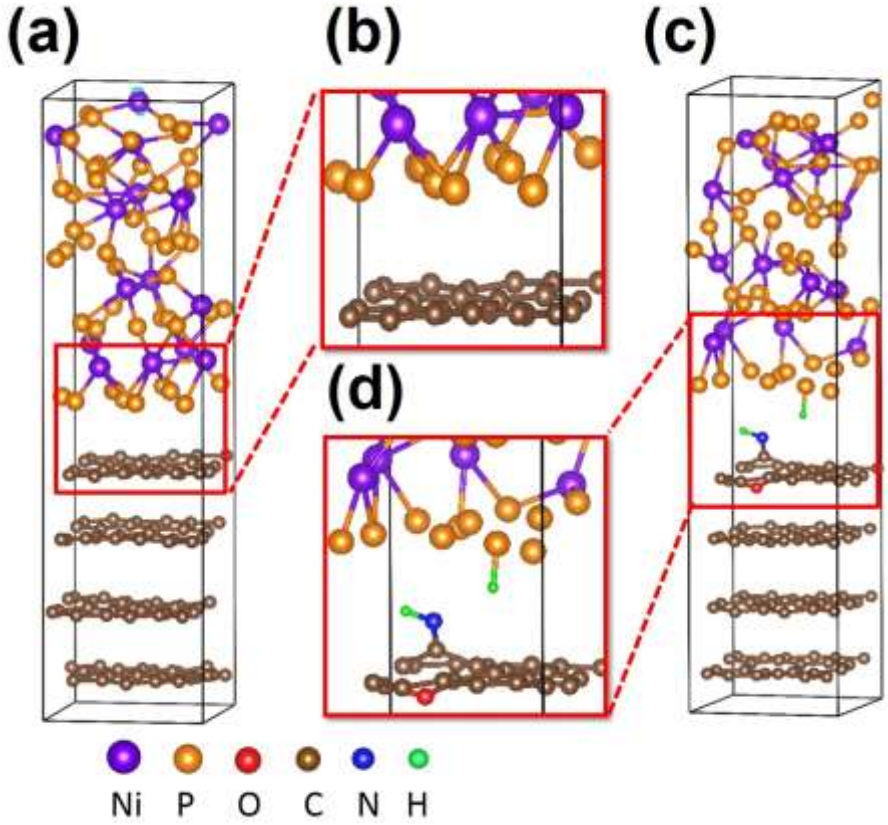

Fig. S17. Snapshots of AIMD simulations taken at 8 ps of (a) NiP_3/pristine graphite and its magnified view (b), and (c) NiP_3/NH_2-graphite and its magnified view (d), with clear indication of no P–C and P–O–C bonds.

References

S1 J. Fullenwarth, A. Darwiche, A. Soares, B. Donnadieu and L. Monconduit, *J. Mater. Chem. A*, 2014, **2**, 2050.
S2 W. J. Li, Q. R. Yang, S. L. Chou, J. Z. Wang and H. K. Liu, *J. Power Sources*, 2015, **294**, 627.
S3 W.-J. Li, S.-L. Chou, J.-Z. Wang, H.-K. Liu and S.-X. Dou, *Chem. Commun.*, 2015, **51**, 3682.
S4 F. Zhao, N. Han, W. Huang, J. Li, H. Ye, F. Chen and Y. Li, *J. Mater. Chem. A*, 2015, **3**, 21754.
S5 S. O. Kim and A. Manthiram, *Chem. Commun.*, 2016, **52**, 4337.
S6 Q.-R. Yang, W.-J. Li, S.-L. Chou, J.-Z. Wang and H.-K. Liu, *RSC Adv.*, 2015, **5**, 80536.
S7 S. O. Kim and A. Manthiram, *Chem. Mater.*, 2016, **28**, 5935.
S8 G.-H. Lee, M. R. Jo, K. Zhang and Y.-M. Kang, *J. Mater. Chem. A*, 2017, **5**, 3683.
S9 J. Song, Z. Yu, M. L. Gordin, S. Hu, R. Yi, D. Tang, T. Walter, M. Regula, D. Choi, X. Li, A. Manivannan and D. Wang, *Nano Lett.*, 2014, **14**, 6329.
S10 G. Kresse and J. Furthmüller, *Phys. Rev. B - Condens. Matter Mater. Phys.*, 1996, **54**, 11169.
S11 P. E. Blöchl, *Phys. Rev. B*, 1994, **50**, 17953.
S12 M. E. Tuckerman, P. J. Ungar, T. Von Rosenvinge and M. L. Klein, 1996, **3654**, 12878.